



## **Climate Variability and Change in Western U.S. Rangelands**

**Arthur M. Greene<sup>1\*</sup> and Richard Seager<sup>2</sup>**

<sup>1</sup>*International Research Institute for Climate and Society, P.O. Box 1000, Palisades NY 10964, United States.*

<sup>2</sup>*Lamont-Doherty Earth Observatory, P.O. Box 1000, Palisades NY 10964, United States.*

### **Authors' contributions**

*This work was carried out in collaboration between both authors. RS suggested the overall scope and objective of the study; AG developed the specific methods, carried out the detailed data analysis and synthesized the conclusions. Both authors have approved the final manuscript.*

### **Article Information**

DOI: 10.9734/IJECC/2020/v10i630204

*Editor(s):*

(1) Dr. Wen-Cheng Liu, National United University, Taiwan.

(2) Dr. Anthony R. Lupo, University of Missouri, USA.

*Reviewers:*

(1) Antipas T. S. Massawe, University of Dar Es Salaam, Tanzania.

(2) Peter Stallinga, University of The Algarve, Portugal.

(3) Adonia K. Kamukasa Bintooro, Nkumba University, Uganda.

Complete Peer review History: <http://www.sdiarticle4.com/review-history/56192>

**Received 23 February 2020**

**Accepted 29 April 2020**

**Published 25 May 2020**

**Original Research Article**

## **ABSTRACT**

We examine variability and change components of precipitation and minimum and maximum daily temperatures, and the derived variables potential evapotranspiration (PET) and the Palmer Drought Severity Index (PDSI), over rangelands in the region 30°-50°N, 100°-125°W. We focus on areas administered by the U.S. Bureau of Land Management (BLM) and Bureau of Indian Affairs (BIA), with a view toward understanding how future climate variations may affect ecosystems, and ultimately, grazing on these lands. Based on an analysis of the annual precipitation cycle we adopt a three-season partition for the year, classifying land areas by season of maximum precipitation; this yields a coherent subregional map. Masking with a combined BLM/BIA footprint, we find that in all subregions both tmin and tmax have increased in response to anthropogenic forcing, the rate being generally greater for tmax. Significant precipitation trends are not detected, whereas PET exhibits significant upward trends in all regions. While PET-normalized precipitation, as well as

\*Corresponding author: E-mail: [amg@iri.columbia.edu](mailto:amg@iri.columbia.edu);

PDSI, do not exhibit significant trends individually (by variable and region), the fact that most trend downward nevertheless suggests a systematic drying. We conclude that temperature constitutes the principal detectable control on hydroclimatic changes in rangelands within the study area. Although ecosystem responses may be complex, future temperature increases are expected generally to reduce soil water availability. The unforced component of variability is investigated with respect to several key climate indices on both interannual and decadal time scales.

*Keywords: Rangelands; grazing; Western U.S.; climate; climate variability.*

## 1 INTRODUCTION

The United States Bureau of Land Management administers grazing rights on about 155 million acres, mostly in the American west. This represents ca. 80% of all western BLM lands, and indeed, grazing represents the primary use of these lands. Grazing activity is managed through a system involving nearly 18000 permits and more than 21000 grazing allotments, mostly for cattle and sheep. These lands also support populations of wild horses and burros. Totals in 2014 were approximately 1.5 million cattle and nearly 50000 wild horses, for a domestic:feral ratio of 30:1 (<http://www.fs.fed.us/rangelands/ftp/docs/-GrazingStatisticalSummaryFY2014.pdf>).

We assess climate variability and change in rangelands administered by the BLM and BIA since 1901, as a first step in evaluating the degree to which current grazing populations and supporting ecosystems may be affected going forward in light of expected increases in global temperatures and other climatic changes in coming decades [1]. Variability is assessed in terms of both anthropogenically forced and naturally occurring variations. For the former we investigate the degree to which local temperature changes are associated with those in global mean temperature; for the latter we consider several large-scale modes of oceanic variability known to influence local climates [2, 3, 4, 5, 6, 7]. Vegetation ultimately depends not on rainfall per se but on soil moisture, which has a significant temperature dependence: shifts in temperature will propagate to water availability aside from any concomitant changes in precipitation. Thus we also consider two temperature-dependent measures of aridity, potential evapotranspiration

(PET) [8] and the Palmer Drought Severity Index (PDSI) [9].

Since the translation of climatic shifts in terms of ecosystem responses is complex, and dependent as well on additional factors (prior conditions, soils, extant plant and animal communities, and so on) [8] we can only provide a general idea of how projected shifts may play out in the ecological sphere. We suggest a modeling pathway for further clarification in this regard.

The aim of this paper is thus to present key features of climate variability and change over BLM and BIA lands as observed during the 20th, and first decade and a half of the 21st, centuries, and based on that analysis to suggest likely inferences for the hydroclimatic future of these key areas.

## 2 MATERIAL AND METHODS

### 2.1 Synopsis

Using both observational and model-generated data (Section 2.2), we carry out a range of procedures. We differentiate between anthropogenic (i.e., human-caused) and naturally-occurring variation, using a straightforward linear regression technique (Section 2.3). The study area is partitioned into subregions using a cluster analysis, based on the season in which the greatest fraction of annual rainfall is received. In a departure from traditional practice, seasonal definitions are implemented using principal components analysis (PCA) applied to the seasonal cycle over the study area, which comprises the continental U.S. west of 100°W and lying between 30° and 50°N (Section 2.4). Climate analysis is carried

out over this full domain, rangelands impacts then being computed by masking to the (combined) BLM/BIA region (Sections 2.5, 3.1).

In addition to precipitation and the monthly means of daily maximum and minimum temperatures, which constitute our primary variables, we consider two derived measures of aridity, PET and PDSI (Section 3.2). We proceed to an examination of remote influences forced by large-scale modes of climate variability, on both interannual and decadal time scales (Sections 3.3, 3.4), including a brief digression into the the far-field sea-surface temperature (SST) and atmospheric characteristics of these modes and their specific impacts on regional precipitation (Section 3.6). Finally we generate a set of subregionally-specific projections, using the statistical relations derived in Section 3.1.

## 2.2 Data

### 2.2.1 Observations

We utilized bias-corrected regional climate data [A. P. Williams, pers. comm., Jan 2019]. Original sources comprise several datasets, including ClimGrid [10] for precipitation and TOPOWX [11] for tmax and tmin. The derived variables PET and PDSI were also provided, additional fields having been utilized for their computation. These include saturation vapor pressure (also from TOPOWX), ambient vapor pressure from the PRISM dataset [12] and wind speed and insolation from the GLDAS2 and NLDAS2 datasets (<http://hydro1.gesdisc.eosdis.nasa.gov/data/>, accessed 2019-01-03). The data were provided and utilized at a uniform resolution of  $0.25^\circ$  [A. P. Williams, pers. comm., Jan 2019]. To evaluate remote influence of large-scale oceanic modes we obtained the NINO3.4 index, based on the HadSST1 dataset [13], from the IRI data library (<https://iridl.ldeo.columbia.edu/SOURCES/.Indices/.nino/.EXTENDED/.NINO34/>) and indices for the Pacific Decadal Oscillation (PDO) [14] and Atlantic Multidecadal Oscillation (AMO), based on the Kaplan dataset [15] from the NOAA Earth Systems Research Laboratory, Physical Sciences Division (<https://www.esrl.noaa.gov/psd/data/climate-indices/>, accessed 2018-10-16). Values for

the 200-mb geopotential height field were taken from the Twentieth-century Reanalysis [16]. A global mean temperature dataset was obtained from the NASA Goddard Institute for Space Studies (GISTEMP Team; <https://data.giss.nasa.gov/gistemp/>, accessed 2018-10-16) [17]. The time period 1901–2016 is utilized for all observational data.

### 2.2.2 Model Simulations

We utilize simulations from the Coupled Model Intercomparison Project, Phase 5 (CMIP5), described in the Fifth Assessment Report of the Intergovernmental Panel on Climate Change (IPCC) [1]. Extensive evaluations have been carried out of North American climate as represented in these simulations, from the perspective of historical climatology [18], historical variability on seasonal to decadal time scales [19] and 21st-century projections [20]. We utilize a global-mean, multimodel mean temperature index (Section 2) to estimate regional sensitivities to anthropogenically-forced climate change, the inferred relations being used to project “near-term” regional climate changes. The temperature index is computed over the period 1901–2041, the 1901–2016 period being used for estimation and the projections extending over the succeeding 25 years. Regional CMIP5 values for tmin and tmax are also utilized, for comparison with these statistically-based projections. Regional CMIP5-based PDSI fields, computed offline (B. Cook, pers. comm. Jan 2019) [43], are also utilized for this purpose. A list of the models utilized appears in Table 1.

## 2.3 Identification of Human-driven Climate Change

Natural, unforced fluctuations among the models can be expected to be mutually incoherent (i.e., uncorrelated), since, by construction, they are not “coordinated” across models by any external driving force. They thus tend, in the multimodel mean, to cancel. To the extent that the models are driven by an imposed external forcing, on the other hand, their responses would be expected to be similar. Thus the global multimodel mean temperature ( $T_{mmm}$ ) can be thought of as

a best estimate, given the size of the ensemble spread about the mean model ensemble, of the Earth's response to as an estimate of the magnitude of climate forcing (primarily increasing atmospheric natural, or *unforced* climatic concentrations of greenhouse gases) and the fluctuations.

**Table 1. Climate models utilized in the construction of the signal shown in Figure . Model resolution in degrees is given as latitude/longitude (for spectral models this corresponds approximately to the study location)**

Modeling center	Model	Resolution
Commonwealth Scientific and Industrial Research Organization (CSIRO) and Bureau of Meteorology (BOM), Australia	ACCESS1-0	1.250/1.875
—	ACCESS1-3	1.250/1.875
Beijing Climate Center, China Meteorological Administration	BCC-CMS1.1	2.791/2.813
—	BCC-CMS1.1(m)	1.122/1.125
Canadian Centre for Climate Modelling and Analysis	CanESM2	2.791/2.813
National Center for Atmospheric Research, USA	CCSM4	0.942/1.250
Centre National de Recherches Météorologiques / Centre Européen de Recherche et Formation Avancée en Calcul Scientifique	CNRM-CM5	1.401/1.401
Commonwealth Scientific and Industrial Research Organization in collaboration with Queensland Climate Change Centre of Excellence	CSIRO-Mk3.6.0	1.865/1.875
LASG, Institute of Atmospheric Physics, Chinese Academy of Sciences and CESS, Tsinghua University	FGOALS-g2	2.791/2.813
—	FGOALS-s2	1.659/2.813
The First Institute of Oceanography, SOA, China	FIO-ESM	2.791/2.813
NOAA Geophysical Fluid Dynamics Laboratory, USA	GFDL-CM3	2.000/2.500
—	GFDL-ESM2G	2.022/2.500
—	GFDL-ESM2M	2.022/2.500
NASA Goddard Institute for Space Studies, USA	GISS-E2-H	2.000/2.500
—	GISS-E2-R	2.000/2.500
Met Office Hadley Centre (additional HadGEM2-ES realizations contributed by Instituto Nacional de Pesquisas Espaciais)	HadGEM2-CC	1.250/1.875
—	HadGEM2-ES	1.250/1.875
Institute for Numerical Mathematics, Russian Academy of Sciences	INM-CM4	1.500/2.000
Institut Pierre-Simon Laplace, France	IPSL-CM5A-LR	1.895/3.750
—	IPSL-CM5A-MR	1.268/2.500
—	IPSL-CM5B-LR	1.895/3.750
Atmosphere and Ocean Research Institute (The University of Tokyo), National Institute for Environmental Studies and Japan Agency for Marine-Earth Science and Technology	MIROC4h	0.562/0.563
—	MIROC5	1.401/1.401
Japan Agency for Marine-Earth Science and Technology, Atmosphere and Ocean Research Institute (The University of Tokyo), and National Institute for Environmental Studies	MIROC-ESM	2.791/2.813
—	MIROC-ESM-CHEM	2.791/2.813
Max-Planck-Institut für Meteorologie	MPI-ESM-LR	1.865/1.875
—	MPI-ESM-MR	1.865/1.875
—	MPI-ESM-P	1.865/1.875
Meteorological Research Institute, Japan	MRI-CGCM3	1.121/1.125
Norwegian Climate Centre	NorESM1-M	1.895/2.500

A multimodel mean, global mean temperature index can thus be taken as the modeled *global* response to imposed radiative forcing. Our index, based on historical simulations through 2005 followed by the RCP8.5 scenario, a “business-as-usual,” or high-emissions trajectory, is shown in Figure along with the GISTEMP annual-mean Land-Ocean Temperature Index, a high-quality observational record. It is clear that over the 1901-2016 observational period Tmmm reproduces quite closely the observed trajectory. As noted above, the model index is extended for an additional 25 years in order to provide a basis for projections (Section 3.7). Using a global rather than a regional index decreases statistical uncertainty, minimizing possible effects of regional deviations. As discussed in [18, 19], even when multimodel mean fields provide close approximations to observed regional climate characteristics, individual model behavior may vary considerably on these scales. We emphasize that the climate model (i.e., CMIP5) simulations employed for projection purposes are utilized only in the global ensemble mean, as

described above. Regional model fields are utilized for comparison with the statistically-based projections.

Forward projections are possible because Tmmm comprises not just past, but also future values. Such projections, however, are contingent on a stationarity assumption, viz., that statistical relationships between global mean temperature and local climate variables remain stable. This calls for prudence in setting the temporal reach of projections, which we limit here to 25 years.

## 2.4 Seasonal Partition

Fig. 2a shows the first three empirical orthogonal functions (EOFs) of the annual cycle of precipitation, which explain 87%, 8.9% and 2.3% of variance in the data, respectively. Figures 2b, 2c and 2d show the corresponding PCs. This analysis identifies the most important temporal patterns in the annual cycle and their corresponding expressions in space.

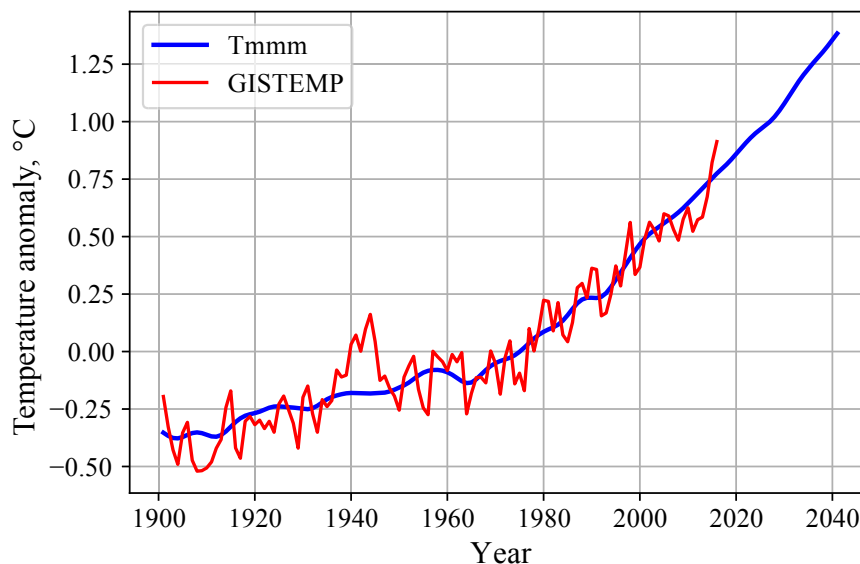


**Fig. 1. The global-mean, multimodel mean index utilized for detrending (Tmmm), shown with the GISTEMP Land-Ocean Temperature Index. GISTEMP is a high-quality observational record**

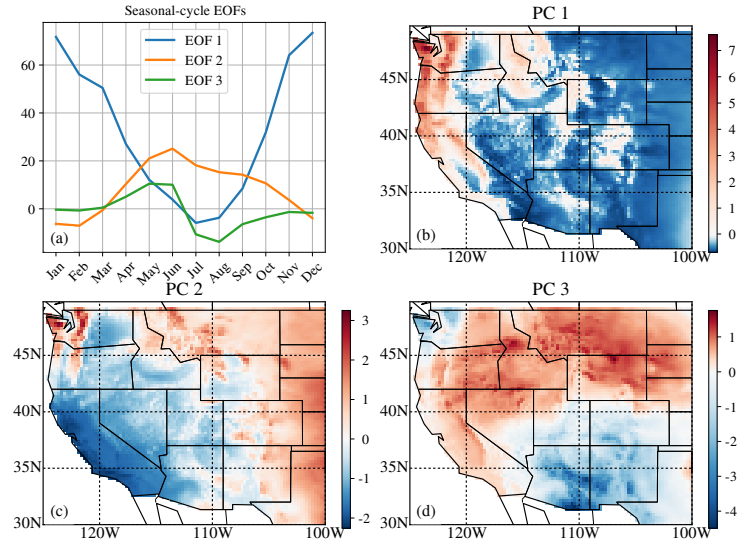


**Fig. 2.** The first three EOFs of the seasonal cycle (a), and the associated PCs (b-d). The patterns are computed over the full data range, 1901-2016. Units for the EOFs are  $\text{mm mo}^{-1}$ ; the PCs are normalized so as to have unit variance

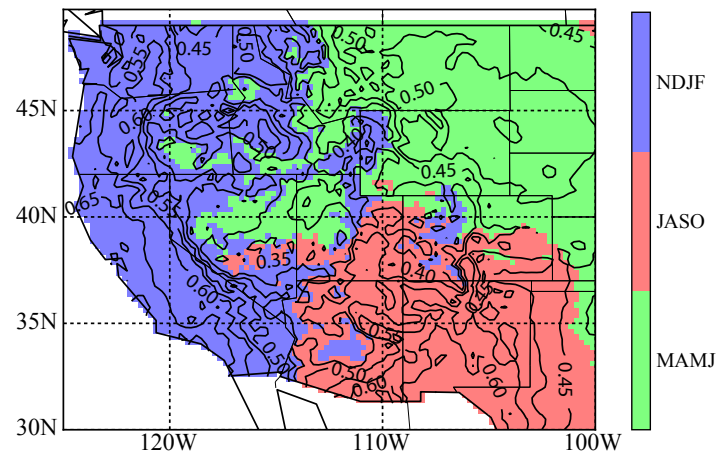


**Fig. 3.** Regional partitioning according to the four-month season having the greatest share of annual precipitation. Contours show the fraction of annual precipitation accounted for by the mapped season

Based on the breadth of the EOF 1 winter peak, a four-month season (NDJF) is first defined. Since the precipitation-based comparison (to follow) is most comprehensible when the seasonal lengths are equal, we complete the annual partition with MAMJ and JASO. While it is less straightforward to map EOFs 2 and 3 into precise seasonal definitions, the identification of MAMJ and JASO with spring and summer, as well as the July boundary separating them, accords well with both the early summer peak of EOF 2 and the abrupt June-July transition of EOF 3. As we will see, these definitions result in well-separated climatologies.

We then identify subregions based on the season, among the three defined, that accounts locally for the greatest fraction of total annual precipitation. In this relatively dry part of the continent, given a stable temperature regime precipitation constitutes the dominant control on vegetative biomass production [21]. We thus focus, in each locality, on the wettest part of the year. A map of these seasonal affinities is shown in Figure 3, where it can be seen that the study area has been partitioned into three more-or-less contiguous zones.

As a check, Figure 4 shows the seasonal cycle of precipitation for the three subregions. While not

identical to the three leading EOFs (cf. Figure 2) these cycles do capture a good deal of their structure.

The NDJF-maximum subregion in Figure 3 can be seen to correspond roughly to the area of positive loading on EOF 1; this is to be expected, given the utilization of that pattern in defining the initial season as well as the large fraction of variance explained by the leading EOF. In fact, by construction *each* of the patterns must reflect some aspect of the climatological seasonal cycle. Thus, the NDJF region corresponds to the coastal and mountain regions with climatological winter precipitation maxima, the JASO region with areas under the influence of the North American Monsoon [22] and the spring (MAMJ) maximum region to interior areas shielded from westerly-borne winter precipitation.

## 2.5 Masking to the BLM/BIA Footprint

Figure 5 shows the locations of BLM and BIA lands, as well as the regional/seasonal partition discussed above and shown in Figure 3, but now masked to the combined BLM/BIA footprint. We examine climatologies, climatic changes and unforced variations within each of the masked seasonal-maxima areas.

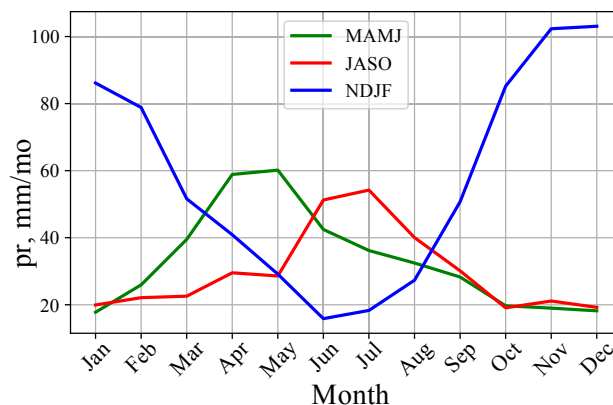
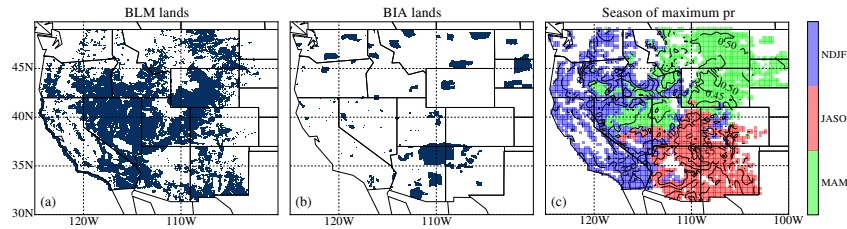


Fig. 4. Deconstruction of the precipitation seasonal cycle. The seasonal cycle of precipitation in each of the climate-defined subregions



**Fig. 5. The regional partition, masked to the BLM/BIA footprint. BLM and BIA lands (a and b, respectively) and the regional partition of Figure 3, masked to their combined footprint (c)**

### 3 RESULTS

#### 3.1 Regional-mean Time Series

Figure 6 shows time series for precipitation,  $t_{max}$  and  $t_{min}$  for each of the subregions, masked to the combined BLM/BIA footprint and for the season of maximum precipitation. Each series has been linearly regressed on the global Tmmm sequence, and the fitted regression lines are also shown. Each fitted line reproduces the Tmmm index, scaled and shifted (i.e., linearly transformed) so as to best fit, in the least-squares sense, the corresponding regional climate record.

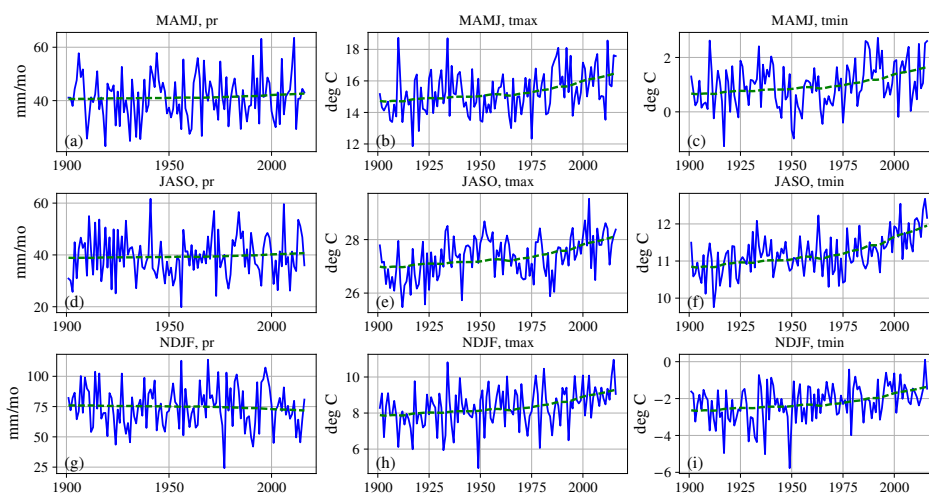
Coefficients and p-values for those regressions are provided in Table 2. None of the precipitation coefficients is statistically significant, so it is not possible to reject the null hypothesis that the regional precipitation variables during the 20th century (seasonalized and masked) do not trend, in terms of their association with the rise in global mean temperature.

The situation is different for both  $t_{max}$  and  $t_{min}$ , both of which show significant responses to changes in global mean temperature. In JASO the coefficients are both very close to unity, implying that changes have been numerically similar to changes in global mean temperature. For  $t_{min}$  in MAMJ, on the other hand, warming has been less, while increases in the remaining three temperature/season combinations have

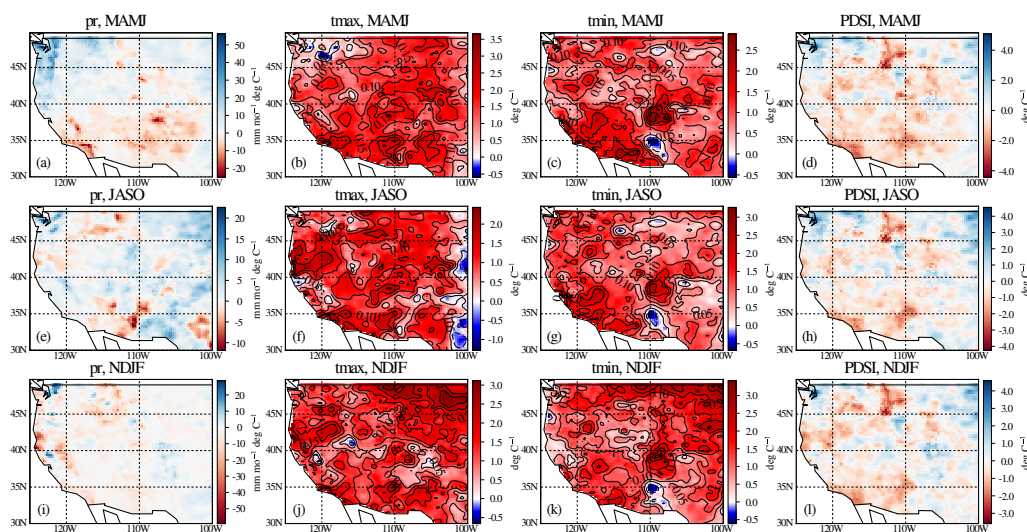
outpaced the global mean. (Note that global *land* temperatures have risen more than those over the oceans; coefficients near unity thus imply warming rates that are somewhat lower than that of the mean global land surface. For consistency when projecting forward, the full global mean is utilized.) For all regions, trends in  $t_{max}$  exceed those in  $t_{min}$ , indicating a general increase in the diurnal temperature range (DTR) over the period of record.<sup>1</sup>

Figure 7 provides a spatially distributed perspective on the series shown in Figure 6, here without the regional or BLM/BIA masks. The area-wide increases in both  $t_{max}$  and  $t_{min}$  are clear throughout the year. While precipitation trends are both weaker and more mixed, the MAMJ plot (Fig. 7a) shows a pattern — drying along the southern tier but moistening to the north — that has been previously documented [24], and which is projected to intensify [25, 26]. Echoes of certain features in the precipitation trend plots — high positive values in the extreme Pacific northwest in all seasons, a concentration of negative values near 30°N, 110°W, particularly in JASO, large-scale N-S dipolar structure in MAMJ, high values to the northeast in JASO — can be identified in the PDSI plots. These suggest that there may be some influence of precipitation change on the evolution of soil moisture, while at the same time reminding us of the relatively low S/N in the precipitation signal.

<sup>1</sup>DTR averaged over the entire domain has undergone large decadal fluctuations over the 20th century, increasing until about 1940, decreasing from then until about 1980 and increasing thereafter. This comports with findings discussed in, e.g., [23].



**Fig. 6. Regional time series for precipitation, tmax and tmin for the three maximum-pr-defined regions, along with fitted regression lines. See text for details**



**Fig. 7. Seasonal trend maps for pr, tmax, tmin, PDSI. These are the variables for which regionalized time series are shown in Figure 6 and for PDSI, and for which the time series are shown in Figure 8. Colors correspond to changes per unit change in global mean temperature. Contours in the tmax and tmin plots show changes in  $\text{deg decade}^{-1}$ . In the first and last columns there are few significant trends, tightly focused on locations of greatest color intensity; for tmax and tmin most trends are significant ( $p = 0.05$ )**

**Table 2. Coefficients and p-values for precipitation, tmax and tmin, regressed on the multimodel temperature index. Units for the pr coefficients are mm mo<sup>-1</sup> per degree global mean temperature change. For tmax and tmin the units would be degrees regional temperature change per degree global mean temperature change, which is dimensionless**

Region (Season)	pr		tmax		tmin	
	coeff	p-val	coeff	p-val	coeff	p-val
MAMJ	1.75	0.48	1.55	7.7e-5	0.86	2.3e-4
JASO	1.59	0.51	1.01	2.9e-6	0.98	6.5e-12
NDJF	-3.60	0.48	1.24	5.5e-5	1.13	7.9e-5

### 3.2 Measures of Aridity: PDSI and PET

Ultimately it is the moisture available to plants that determines vegetative characteristics, for which we examine potential evapotranspiration (PET) and PDSI, variables that are derived, rather than measured directly. The former, which characterizes the moisture that the atmosphere could extract from a well-watered surface, is used to normalize precipitation. PDSI, computed with the aid of a water balance model (thus not completely independent of PET) is a more direct proxy for soil moisture and serves as an alternate way to gauge water availability [27].

Figure 8 shows time series of PET, precipitation/PET and PDSI for the precipitation-defined regions, where the data have been masked to the BLM/BIA footprint prior to spatial averaging. The consistent upward trends in PET are significant at better than 0.001 for all three regions. Neither the MAMJ nor JASO trends in pr/PET, the former downward and the latter nearly flat, are statistically significant, however, while that for NDJF is ( $p = 0.05$ ). This difference can be related, at least in part, to a considerably larger trend in NDJF (-9.1, vs. -3.6 and -2.9 for MAMJ and JASO, respectively) relative to variance, which is similar across regions. Trend differences are also masked here by the change in scale engendered by the larger ratio of precipitation to PET in NDJF than in the two other seasons, nearly an order or magnitude. Further, pr in NDJF trends downward even before normalization by PET. Note that the denominator in pr/PET can be arbitrarily small, increasing variance and making trend detection more difficult.

On an interannual basis pr and PET are anticorrelated, with coefficients -0.55, -0.48 and -0.06 for MAMJ, JASO and NDJF, respectively, reflecting a general inverse relationship between precipitation and surface temperature, at least during the warm part of the year [28, 29]: dry conditions increase the sensible heat flux at the expense of evaporation, increasing the air temperature and thus PET directly.

### 3.3 Time Scale Decomposition

Figure 9 shows the series of Figure 6 with the long-range climate-change trends removed. On each plot, a lowpassed version, obtained by the application of a fifth-order Butterworth filter with half-power point at  $0.1 \text{ yr}^{-1}$ , is superimposed, providing a view of the decadal component of the signal. Subtracting this lowpassed signal in turn yields high-frequency residuals, for which most of the energy resides in the interannual-to-decadal band. As an aid to visualizing this interannual component, values above the lowpass line are plotted as red, those below as blue. Within each region the three variables may thus be assessed on both interannual and decadal time scales, providing a multiscale background for the exploration of remote influences. The southeast (JASO region) drought of the 1950s, e.g., is particularly clear in the corresponding tmax time series, and follows from surface drying [30, 31].

### 3.4 Remote Influences on Regional Climates

Many large-scale modes of climate variability are characterized by variations in SST, which, through the atmosphere, can exert

remote influences on regional climates. The SST variations themselves can be used to construct indices to characterize modal behavior. Here we test our regional climate records against three such indices. Two, the NINO3.4 index, based on the El Niño-Southern Oscillation (ENSO, see <https://www.esrl.noaa.gov/psd/enso/>) and the PDO [14, 32], represent Pacific ocean modes; the third is the AMO [33, 34, 35]. Each of these modes have been implicated as having far-field effects on western US climate [36, 2, 3, 4, 5, 6, 7].

The three index series are shown in Figure 10, seasonalized to correspond with the regional variables. Notable in the NINO3.4 record (labeled simply "NINO") for NDJF (Fig.10g) are peaks in 1983 and 1998, years of strong warm events in the tropical Pacific. (As we have seasonalized the indices here, the assigned record year of the 1982-1983 NDJF season is 1983.) Values of the PDO index reflect, for all the seasons, known low (high) anomalies during the period 1950-1975 (1977-1998), signaling its more prominent low-frequency, or decadal, character as compared with the strong interannual-band energy of ENSO [37]. In the case of the AMO this decadal character is even more pronounced.

### 3.5 Association of Variability with Atmospheric Circulation and SSTs

The correlation maps of Figure 11 provide a larger-scale perspective on the three climate indices and the chain of effects that mediates their influence on western US precipitation. The maps are based on annual mean values; for the PDO and AMO plots (center and rightmost columns) the indices have been lowpass filtered, suppressing responses to interannual variations in favor of the decadal time scale, where

these phenomena have the greatest influence (cf. Fig. 10).

The upper row of plots (Figs. 11a–11c) show correlations with the SST field, key features being for NINO a narrow equatorial zone of warm SSTs extending westward from the South American Coast to approximately the date line, surrounded on the west by a "horseshoe" of SSTs of opposite sign. In the next row (Fig. 11d), we see that positive correlations with the NINO3.4 index correspond to a region of higher-than-normal anomalies above the tropical Pacific in the 200 mb geopotential height field (z200), with low anomalies to the north (these are mirrored in the south), similar to the so-called Pacific-North American (PNA) pattern, a large-scale wave train extending from the Pacific over North America [38]. Finally, in the lower panel (Fig. 11g) we see the effect on precipitation in the western US, namely the enhanced values to the south of approximately 40°S, with reductions to the north.

The PDO signatures are similar to those for NINO, but involve a broadened equatorial warm SST region and enhanced intensity for both SST and z200 in the Northern Pacific, a defining characteristic of this mode. The classical SST signature of the AMO, meanwhile, a basinwide warming of the entire North Atlantic, appears clearly in Figure 11c. The z200 response here is broader than those of either NINO or PDO, tropically centered and hemispherically quasi-symmetric; the effect on study-area precipitation is generally a reduction (Fig. 11i)<sup>2</sup>. For NINO, and to a lesser extent the PDO, the height anomalies indicate stronger (weaker) westerlies entering southwestern (northwestern) North America. This is associated with a southward-shifted Pacific storm track [39, 40] and the wet-dry north-south dipole. The AMO causes anomalous high pressure across the west, reducing precipitation.

---

<sup>2</sup>At interannual time scales the AMO precipitation response is of opposite sign (not shown). We believe, however, that this represents an indirect influence, in which ENSO, which is active principally on interannual time scales, forces the tropical North Atlantic, which in turn drives a positive precipitation response over much of the study area. Further discussion of these teleconnections can be found in the references cited.

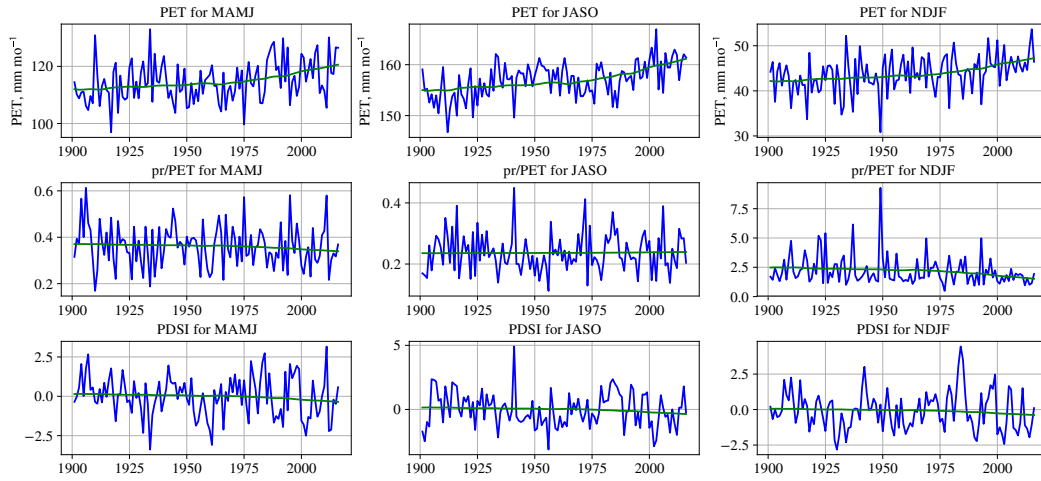


**Fig. 8. Time series for PET, pr/PET and PDSI. Regional time series for potential evapotranspiration (PET), precipitation normalized by PET and PDSI, for the three maximum-precipitation-defined regions. Values were masked to the BLM/BIA footprint. pr/PET and PDSI are dimensionless**

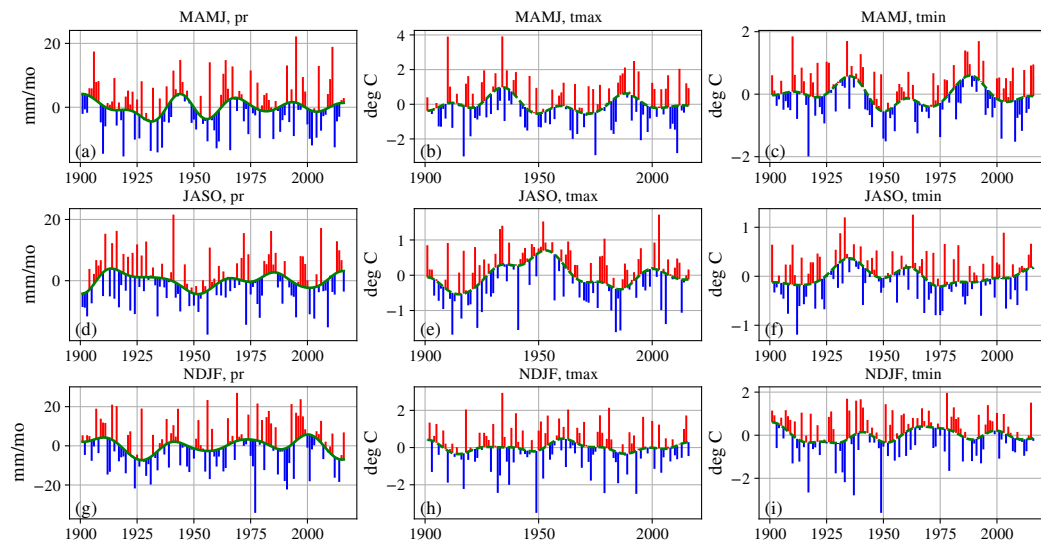


**Fig. 9. Detrended regional time series for precipitation, tmax and tmin, for the three maximum-precipitation-defined regions. Lowpassed versions are superimposed. Values above the lowpass line are shown as red, those below as blue, in order to better visualize the interannual residuals after removing the lowpassed signal**

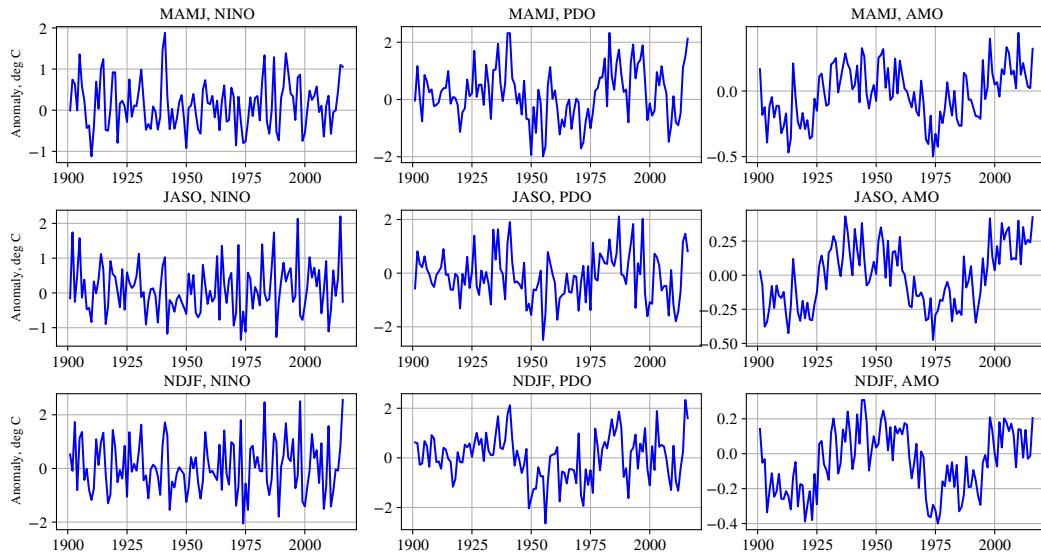


**Fig. 10. Climatic SST indices utilized in the analysis of remote influence. The indices are averaged over the indicated seasons. The NINO3.4 index is an SST (i.e., temperature) anomaly; the others are dimensionless**

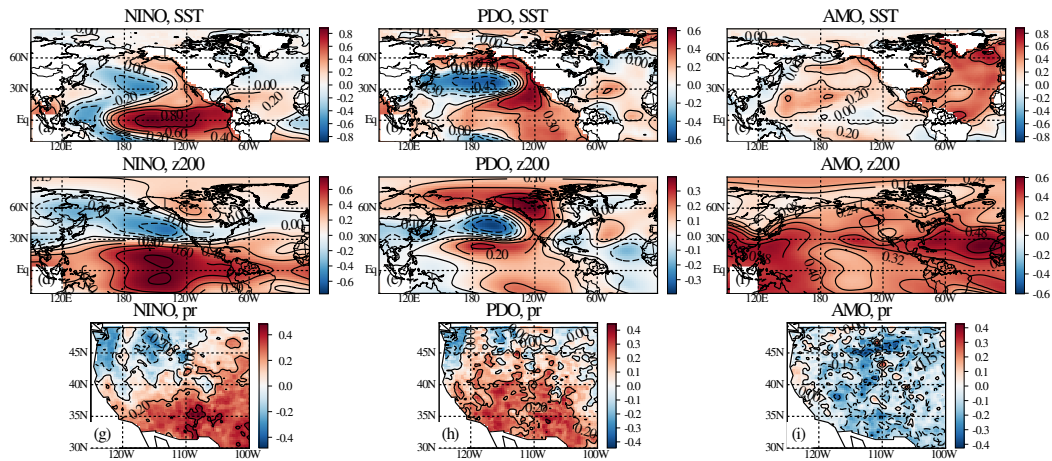


**Fig 11. Correlation maps tracing the chain of remote influence. Maps are shown for the three climate indices investigated and SST (a–c), the 200-mb geopotential height field (d–f) and precipitation over the study area (g–i). All the maps are based on annually-averaged data (both indices and the respective variables); for the PDO and AMO maps the indices have been lowpass-filtered**

### 3.6 Influence of the Large-scale Modes on Regional Precipitation

Figure 12 shows seasonal correlation maps for precipitation and the three climate indices, again utilizing interannual variations for NINO and lowpassed series for PDO and AMO. The maps are stippled where correlations are significant at  $\alpha = 0.05$  (two-sided test). Lowpass filtering introduces temporal dependence, reducing effective degrees of freedom, thus increasing the significance threshold. In this case the relevant values are 0.183 and 0.576, for interannual and 10-year lowpassed correlations, respectively. Because of this, and owing to the fixed record length, decadal-scale correlations are intrinsically more difficult to verify, which is reflected by the sparsity of significant points in the PDO and AMO maps. ENSO and PDO responses show a degree of similarity, a fact that has been previously noted [41, 42].

Several of the NDJF maps, particularly Figure 12g, exhibit dipolar responses, which would mix areas with opposing signs when computing region-averaged correlation coefficients. To avoid this complication we compute, for NDJF only, *two* coefficients, for areas north and south of the 40th parallel, an approximate nodal line (again, most evident in Fig. 12g). Responses in the other regions are primarily of a single sign (cf. Fig. 3).

Table 3 shows correlation coefficients for the three regional/seasonal precipitation, tmax and tmin records and the three correspondingly seasonalized index series, the climate data having been masked to the combined BLM/BIA footprint prior to area-averaging. As with Figures 11 and 12, PDO and AMO indices used for these computations have been lowpassed. Significant coefficients are shown in boldface.

There are just two significant interannual correlations for precipitation, both for NINO: in JASO and NDJF (south). There is also a significant NINO correlation for tmin in MAMJ. In light of the congruence of ENSO and PDO the matching signs for pr and PDO in both JASO and NDJF (both north and south) are also of interest, as are those for tmin in MAMJ. There

are no significant decadal coefficients, although the PDO-NINO agreement is indicative, as are the uniformly negative precipitation responses to AMO [2, 3, 4].

We also performed a reverse analysis, correlating SST fields with regional climate indices. The results (not shown) were generally in agreement, indicating clear ENSO, PDO and AMO influences.

### 3.7 Near-term Climate Change Projections

Figure 13 shows observed temperature and PDSI time series for the three climatically-defined regions, as masked to the BLM/BIA footprint, along with 25-year projections (red lines). For comparison, corresponding records from the CMIP5 ensemble are also shown, extended to match the projections. The idea is to compare the latter, which are obtained by applying the computed 20th-century regression coefficients to future values of Tmmm, with direct outputs from the models. The CMIP5 model runs generally extend through the end of the century (some are longer); the length of these projections has been limited so as to not stray too far from the domain over which the coefficients are computed. As discussed in Section 3.1, coefficients for pr were not significant, so no attempt is made to project that variable. Models do provide some idea of how precipitation may change in the future, however (see., e.g. [25]).

It can be seen from Figure 13 that tmax in all seasons, as well as tmin for JASO, exhibits a cold bias (Table 4 gives the mean observational-period offsets). CMIP5 temperature *trends*, particularly for JASO, also show some biases, the model trends beginning around 1970 being somewhat oversteepened. Biases in PDSI are quite small. This variable is not intrinsic to the models; however, but has been computed (and calibrated) offline [43]. The projections agree in every case with the sense of the CMIP5 trends, the differences amounting to second-order corrections. The projections, by construction, also remove the additive component of the biases evident in the CMIP5 simulations.

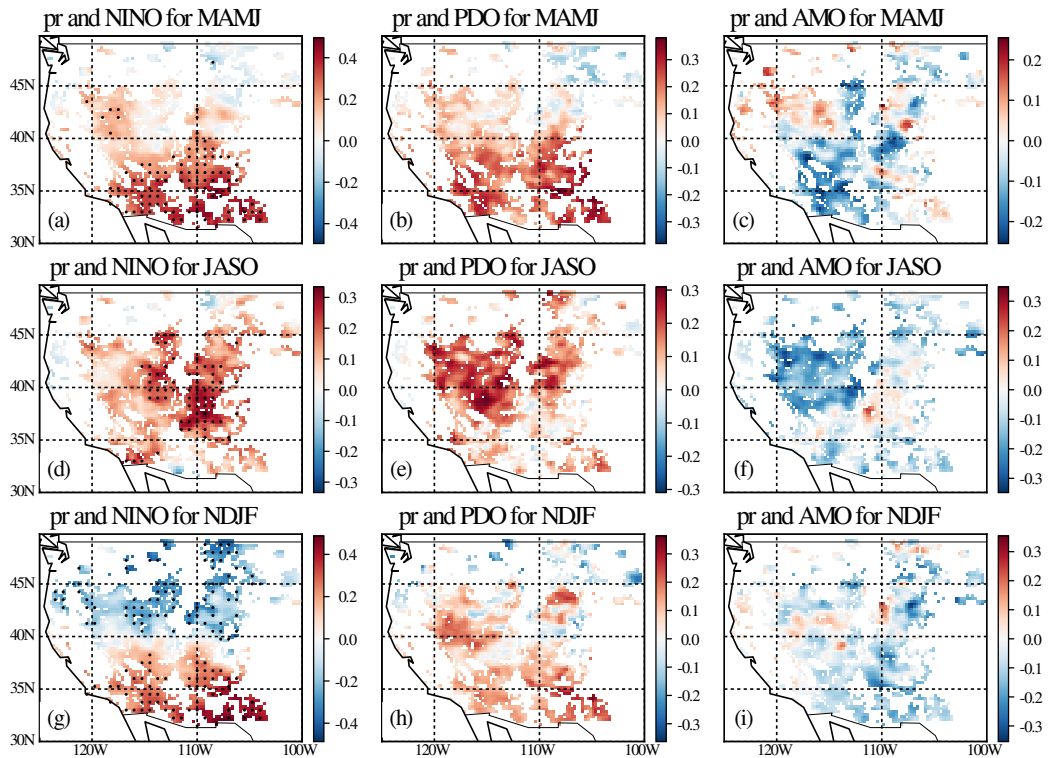


**Fig. 12. Correlation maps for precipitation and climate indices. Maps are shown for precipitation and (a, d, g) NINO3.4, (b, e, h), PDO and (c, f, i), AMO, for MAMJ, JASO and NDJF, respectively. Stippling is applied in areas where significance levels are < 0.05. Interannual (decadal) variations are utilized for NINO (PDO, AMO)**

**Table 3. Correlation coefficients for each of the BLM/BIA-masked regional precipitation, tmax and tmin series with NINO, PDO and AMO indices. For NDJF, values before and after the vertical dividing line within each box refer to areas north and south of the 40th parallel, respectively. As in Figures and , PDO and AMO indices have been lowpass filtered. Values significant at the 0.05 level are shown in boldface**

Index	Season	precip	tmax	tmin
NINO	MAMJ	0.09	0.07	<b>0.21</b>
	JASO	<b>0.23</b>	-0.08	0.02
	NDJF	-0.18   <b>0.24</b>	0.12   -0.11	0.09   0.13
PDO	MAMJ	-0.01	0.26	0.39
	JASO	0.12	-0.20	0.00
	NDJF	-0.10   0.13	-0.08   0.01	-0.09   0.15
AMO	MAMJ	-0.07	0.08	0.01
	JASO	-0.09	0.33	0.25
	NDJF	-0.02   -0.08	0.09   0.04	0.02   -0.07

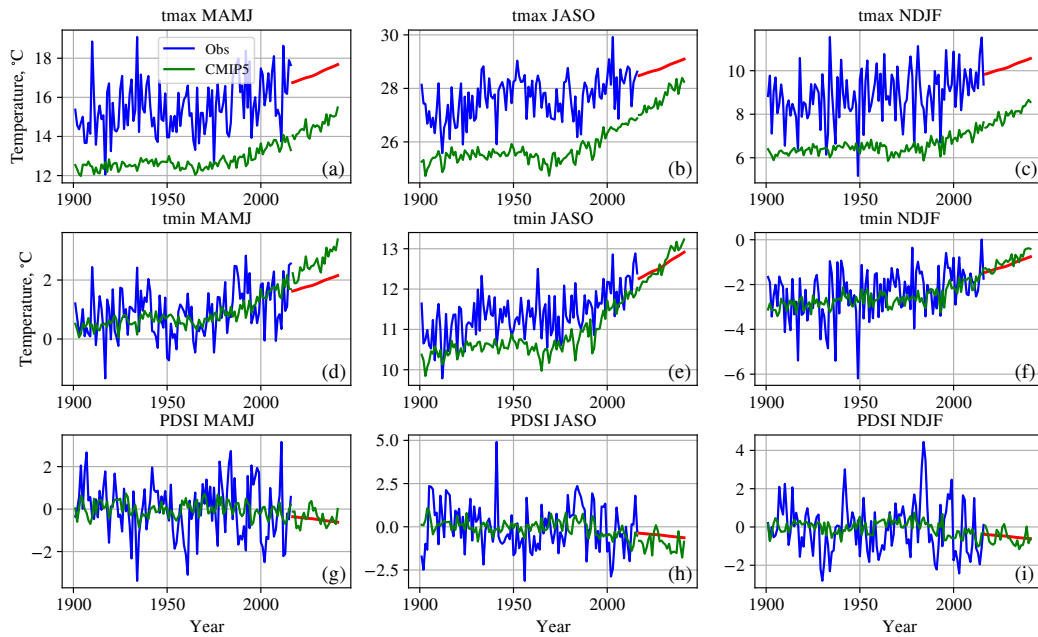


**Fig. 13. Projections for tmax, tmin and PDSI. Twenty-five-year projections (red) are shown for tmax, tmin and PDSI, based on the relationship of these variables to Tmmm over the 1901-2016 period. Green traces, with the exception of PDSI, which is derived from the models ex post facto, are the CMIP5 multimodel mean values. PDSI is dimensionless**

**Table 4. Biases in tmax and tmin in CMIP5 multimodel means for 1901-2016, seasonalized and masked similarly to the observational data to which the model simulations are compared. Units are degrees C**

(Season)	tmax	tmin
MAMJ	-3.07	-0.13
JASO	-1.80	-0.52
NDJF	-2.44	-0.34

**Table 5. Projected shifts, by region, in tmax, tmin and PDSI. Values for the first two of these are given in degrees C; PDSI [27] is dimensionless**

(Season)	tmax	tmin	PDSI
MAMJ	1.29	0.67	-0.49
JASO	1.07	1.05	-0.69
NDJF	1.19	1.01	-0.62

The upward trends projected for tmax and tmin, and inverse trends in PDSI, are not surprising, given the relationships established in Section 3.1 and shown in Table 2, along with the well-defined future tendency of Tmmm (Fig. 1). Mean changes between the standard 1980-2010 climatological period and projections for the 2031-2040 decade, by region, are given in

Table 5. These shifts, averaging 1.05°C for  $t_{max}$  and  $t_{min}$  over all seasons, and -0.60 in PDSI, are substantial, and can be expected to have measurable impacts.

Owing to the use of a multimodel-mean record for their computation, both the projections and CMIP5 values lack the strong variability evident in the 20th-century records. (Variability in the former is additionally suppressed because it is a global, rather than a regional mean.) This does not imply that future climate will be characterized by such low variance. Indeed, natural variations will continue, with teleconnections to the large-scale modes creating a complex spatiotemporal background against which forced changes will play out.

## 4 DISCUSSION AND CONCLUSIONS

### 4.1 General Implications

Given the observational statistics and the methods utilized, relations between global mean temperature, in the form of  $T_{mmm}$ , and the primary regional variables can be established only for  $t_{max}$  and  $t_{min}$ . The lower S/N ratio of precipitation generally, as compared with temperature variables, has frequently been remarked [1], so this is not a surprising finding. In an examination of future precipitation changes in CMIP5, also utilizing the RCP8.5 experiment, [20] determined that multimodel ensemble mean changes across most of the study were significant. That assessment, performed entirely within the model domain, compared the 2070–2099 period with 1961–1990 climatological means and utilized precipitation amounts directly (rather than dependencies on  $T_{mmm}$ ), so it is not strictly comparable with what we have done here. According to [20], the CMIP5 models indicate that by the end of the present century our entire domain will have reduced precipitation during JJA; for DJF a dipolar shift is projected, with moistening to the north of about 35°N and drying to the south (Fig. 1 in [20]).

Despite the lack of significant  $T_{mmm}$ -precipitation relations in our analysis it is

nonetheless true that temperature, through its effects on atmospheric moisture demand, thus evapotranspiration, and potentially also on land-surface processes, exercises an important control on soil water availability. The net effect of rising regional temperatures during the observational period, as estimated via the indirect variable PDSI as well as  $pr/PET$ , has been a reduction in soil moisture. This effect is consistent across the seasonally-based regions defined herein but is robust with respect to alternate seasonal definitions as well as other metrics, such as precipitation minus evaporation (P-E) [44]. (It is perhaps worth noting that long-term soil moisture data that might be used to verify these observation-based inferences do not exist.)

Using the statistical relations developed during the analysis, simple 25-year regional-scale projections were developed. Owing to the dependence of regional temperatures on the global mean, and the continuing rise projected for the latter, both  $t_{max}$  and  $t_{min}$  are expected to increase, and PDSI to decrease, over the projection time horizon. Comparison with directly modeled regional temperatures show similar trends, but with additive biases in the models, particularly for  $t_{max}$  (the statistical projection method utilized implicitly removes these biases). The expectation is thus that soil water availability in the subject regions, and in particular on BLM/BIA rangelands, will continue to decline in coming decades, likely exacerbated seasonally by reductions in precipitation.

The influence of natural variability was also assessed, particularly with regard to precipitation. Such variability may significantly modulate the identified anthropogenically-driven trends, over periods of years to decades. A primary driver of interannual (i.e., year-to-year) variations was shown to be ENSO, which has long been known to influence North American, and particularly, western, climate. On decadal scales, effects of both Pacific and Atlantic influences, in the form of the PDO and AMO, respectively, were considered. For decadal-varying influences it is difficult to establish grid-level statistical dependence using records of the length of our observational dataset. However these modes have separately been shown

to be influential [34]. None of these natural drivers have (yet) proven to be predictable beyond the time horizon of perhaps a year, but decadal prediction is an active area of research [45, 46, 47, 48].

The projections indicate declining soil water availability, resulting essentially from increases in regional temperature, an outcome reinforced by previous findings [49, 44]. Although no attempt is made to project precipitation changes this should not be taken as a finding that no precipitation change is expected to occur, and indeed, there is some evidence for future seasonal and subregional drying (as well as moistening, see Section 3). However it is simply not possible to assign statistical significance based on the observational records alone.

A starting point, then, is the expectation that the future will see rising temperatures, with  $t_{max}$  in the study regions possibly increasing faster than  $t_{min}$ . Reductions in soil water availability, even in the absence of reductions in precipitation (and likely in their presence), are an expected corollary.

## 4.2 Contribution of Natural Variability

In addition to the anthropogenically-forced response, natural climate system fluctuations can be expected to impose variations, by season, climate variable and time scale, as discussed in Section 3.7. As has been the case during the 20th century, these variations may at times be comparable to, or larger than, the comparatively slow monotonic trends resulting from anthropogenic influence. This situation implies limits to predictability – or at the least a careful consideration of natural climatic “noise” as a component of prediction uncertainty – on more distant time horizons, at least until the science of decadal prediction has become more mature.

## 4.3 Additional Effects

Certain other consequences of increasing temperature are not considered directly but are likely to play a role in future hydroclimatic changes. Important among these are changes in

snowfall and snowpack, and the seasonal cycle of runoff. There is also a general expectation that hydroclimate variability will increase as the globe warms [50]. From the thermodynamic standpoint this owes to the rapid increase of water vapor saturation pressure with temperature. Such an increase may presage changes in the frequency of extreme weather events at both the wet and dry ends of the spectrum, although these events would be occurring relative to an ever-drier soil moisture baseline. In addition there are likely to be dynamically-motivated effects, i.e., changes in atmospheric circulation, that affect both the mean climate and variations about the mean.

## 4.4 Consequences for Eco-Systems

Beyond the direct effects of temperature change on soil water availability, there are many potential indirect and consequent effects and interactions, making detailed inference difficult without some sort of follow-on modeling. We survey some of these effects here.

It is pointed out in [21] that ecosystem changes are in general dependent on antecedent conditions, suggesting a degree of hysteresis, or at least memory. Such changes may also be asymmetric, since the demise of some species may be more or less rapid than the establishment of replacements. Aside from the availability of suitable habitats, establishment of new species is also constrained by seed dispersal mechanisms (wind, insects, birds) and their respective environmental controls.

Based on the same increase in atmospheric carbon dioxide ( $CO_2$ ) that drives global temperature changes, a fertilization effect is expected, which may offset to some extent the direct effects of drying by increasing the water-use efficiency of plants. Counterintuitively,  $CO_2$  fertilization, by shifting the partitioning of water toward plant utilization and away from runoff, may also act to increase leaf area, producing a “greening,” even in the face of drying ([51, 52] and references cited therein). Increases in net primary production (NPP) are dependent not only on  $CO_2$  but on the availability of nutrients, which may prove in some cases to be limiting [53].

The declining values of PDSI, as a function of both time and global temperature (Fig. 8) suggest that the future pathway in all of our BLM/BIA seasonal regions will be toward *reduced* soil water availability. Thus future changes are likely to occur on a fundamental level. Clearly, however, attempting to project these and other complex responses and gauge their effects on grazing potential in a region of even limited extent would require the deployment of well-calibrated hydrology, ecosystem and grazing models, perhaps coupled to a climate generator. (An agricultural prototype is discussed in [28]). Such analysis lies beyond the scope of the present research.

#### 4.5 Strategic and Policy Recommendations

Many considerations come into play when considering possible pathways for mitigation and/or adaptation measures. Among them are national agricultural, economic and recreational priorities, stakeholder interests, ecosystem impacts and larger questions of sustainability. These considerations involve potentially competing values, and not all share a common decision time frame. Striking a balance among them will also involve factors at the strategic level, and, given the conclusions of this research, a balance will evidently have to be achieved against a slowly but inexorably drying background state for the decades ahead. Developing a program of specific recommendations is itself a complex problem deserving of careful study and analysis. Very broadly, overall environmental health, and the sustainability of natural landscapes, species diversity and ecosystems must be prioritized. These factors underpin all uses, including grazing, to which these rangelands may be put.

More specifically with respect to grazing, projected declines in soil water availability imply a concomitant loss of carrying capacity. A conservative policy choice in this case might be to modify grazing allotments in accordance with confirmed shifts in forage availability. Since changes are not likely to be spatially uniform and will fall across a variety of landscape features, such reductions will necessarily be

adaptive, taking into account the interplay between landscape morphology, geology, soil typologies and the local pattern of hydrological shifts.

With respect to the expected primary reductions in soil water availability per se, it *might* be feasible to ameliorate these to a degree via direct ecosystem intervention, for example by planting, or at least encouraging the growth of, drought-tolerant forage options. Such a strategy will ultimately require both modeling and in-situ testing, first to determine feasibility, and then for optimization. In the end, specific policy choices will be governed by the balance of potentially competing priorities described above.

## 5 IMPLICATIONS

It is likely that the American West, including BLM and BIA lands therein, will experience reductions in soil water availability as the planet continues to warm in coming years and decades. Indeed, it is likely that such reductions have already begun, accelerating during the second half of the 20th century. This is most easily verifiable, from the statistical standpoint, as a consequence of increasing temperatures, rather than reductions in precipitation, although future changes in the latter are certainly within the realm of possibility [20]. The observed regional temperature increases can be sensibly related to the well-understood anthropogenically driven rise in global mean temperature, particularly during the latter part of the observation period.

The reduction in available soil water may well result in a decrease in forage availability, thus grazing capacity, on BLM and BIA lands. However ecosystems and the potential interactions among effects are complex, and we have seen that counterintuitive responses (e.g., increases in leaf area at the same time that soils are drying) are possible. More definitive projections await the application of suitable models, driven by downscaled and elaborated climate projections (preferably accompanied by uncertainty estimates). Such an elucidation constitutes a logical next step in this work.

## ACKNOWLEDGMENT

We express thanks to A. Park Williams, of the Lamont-Doherty Earth Observatory, for providing the derived PET and PDSI fields as well as assistance with the ClimGrid data, and to Ben Cook, of the NASA Goddard Institute for Space Studies, for providing the CMIP5 PDSI model fields. This work was supported by the National Science Foundation (award AGS 1243204, "Linking near-term future changes in weather and hydroclimate in western North America to adaptation for ecosystem and water management.") This is L-DEO contribution #8484.

## COMPETING INTERESTS

The authors declare that no competing or conflicting interests exist.

## REFERENCES

- [1] Stocker T, Qin D, Plattner GK, Tignor M, Allen S, Boschung J, et al., Eds. Climate change 2013: The physical science basis. Contribution of working group I to the fifth assessment report of the intergovernmental panel on climate change. Cambridge, United Kingdom and New York, NY, USA: Cambridge University Press. 2013;1535. DOI: 10.1017/CBO9781107415324
- [2] Enfield DB, Mestas-Nunez AM, Trimble PJ. The Atlantic multidecadal oscillation and its relation to rainfall and river flows in the continental U.S. In: Geophys. Res. Lett. 2001;28(10):20772080. DOI: 10.1029/2000GL012745
- [3] Sutton RT, Hodson, DLR. Atlantic Ocean forcing of North American and European summer climate. In: Science. 2005;309(5731):115118. DOI: 10.1126/science.1109496
- [4] McCabe GJ, Palecki MA, Betancourt JL. Pacific and Atlantic Ocean influences on multidecadal drought frequency in the United States. In: P. Natl. Acad. Sci. 2004;101(12):41364141. DOI: 10.1073/pnas.0306738101
- [5] McPhaden MJ, Zebiak SE, Glantz MH. ENSO as an integrating concept in earth science. In: Science. 2006;314(5806):17401745. DOI: 10.1126/science.1132588
- [6] Kushnir Y, Seager R, Ting M, Naik N, Nakamura J. Mechanisms of tropical Atlantic SST influence on North American precipitation variability. In: J. Climate. 2010;23(21):56105628. DOI: 10.1175/2010JCLI3172.1
- [7] Meehl GA, Hu A, Arblaster JM, Fasullo J, Trenberth KE. Externally forced and internally generated decadal climate variability associated with the interdecadal Pacific oscillation. In: J. Climate. 2013;26(18):72987310. DOI: 10.1175/JCLI-D-12-00548.1
- [8] Bonan G. Ecological climatology. U.K.: Cambridge; 2002.
- [9] Palmer WC. Meteorological drought. Research Paper 45. Washington, D.C.: Office of Climatology, U.S. Weather Bureau;1965.
- [10] Vose RS, Applequist S, Squires M, Durre I, Menne MJ, Claude N. Williams J, et al. Improved historical temperature and precipitation time series for U.S. climate divisions. In: J. Appl. Meteorol. Climatol. 2014;53:12321251. DOI: 10.1175/JAMC-D-13-0248.1
- [11] Oyler JW, Ballantyne A, Jencso K, Sweet M, Running SW. Creating a topoclimatic daily air temperature dataset for the conterminous United States using homogenized station data and remotely sensed land skin temperature. In: Int. J. Climatol. 2015;35(9):22582279. DOI: 10.1002/joc.4127
- [12] Daly C, Halbleib M, Smith JI, Gibson WP, Doggett MK, Taylor GH, et al. Physiographically sensitive mapping of climatological temperature and precipitation across the conterminous United States. In: Int. J. Climatol. 2008;28(15):20312064. DOI: 10.1002/joc.1688
- [13] Rayner NA, Parker DE, Horton EB, Folland CK, Alexander LV, Rowell DP, et al. Global analyses of sea surface temperature, sea ice and night marine air temperature since

- the late nineteenth century. In: *J. Geophys. Res.* 2003;108(D14):4407.  
DOI: 10.1029/2002JD002670
- [14] Mantua NJ, Hare SR, Zhang Y, Wallace JM, Francis RC. A Pacific interdecadal climate oscillation with impacts on salmon production. In: *Bull. Am. Met. Soc.* 1997;78(6):10691079.  
DOI: 10.1175/1520-0477(1997)078;1069:APICOW;2.0.CO;2
- [15] Kaplan AM, Cane M, Kushnir Y, Clement A, Blumenthal M, Rajagopalan B. Analyses of global sea surface temperature 1856- 1991. In: *J. Geophys. Res.* 1998;103(18):567589.
- [16] Compo GP, Whitaker JS, Sardeshmukh PD. Feasibility of a 100 year reanalysis using only surface pressure data. In: *Bull. Am. Meteorol. Soc.* 2006;87:175190.  
DOI: 10.1175/BAMS-87- 2- 175
- [17] Hansen J, Ruedy R, Sato M, Lo K. Global surface temperature change. In: *Rev. Geophys.* 2010;48:RG4004.  
DOI: 10.1029/2010RG000345
- [18] Sheffield J, Barrett AP, Colle B, Nelun Fernando D, Fu R, Geil KL, et al. North American climate in CMIP5 experiments. Part I: evaluation of historical simulations of continental and regional climatology. In: *J. Climate.* 2013;26(23):92099245.  
DOI: 10.1175/JCLI-D- 12-00592.1
- [19] Sheffield J, Camargo SJ, Fu R, Hu Q, Jiang X, Johnson N, et al. North American climate in CMIP5 experiments. Part II: evaluation of historical simulations of intraseasonal to decadal variability. In: *J. Climate.* 2013;26(23):92479290.  
DOI: 10.1175/JCLI-D-12- 00593.1
- [20] Maloney ED, Camargo SJ, Chang E, Colle B, Fu R, Geil KL, et al. North American climate in CMIP5 experiments: Part III: Assessment of twenty-first-century projections. In: *J. Climate.* 2014;27(6):22302270.  
DOI: 10.1175/JCLI-D-13-00273.1
- [21] Polley HW, Briske DD, Morgan JA, Wolter K, Bailey DW, Brown JR. Climate change and North American Rangelands: Trends, projections, and implications. In: *Rangeland Ecol. Manage.* 2013;66(5):493511.  
DOI: 10.2111/REM-D-12-00068.1
- [22] Adams DK, Comrie AC. The North American monsoon. In: *Bull. Am. Meteorol. Soc.* 1997;78(10):21972214.  
DOI: 10.1175/1520-0477(1997)078;2197:TNAM;2.0.CO;2
- [23] Vose RS, Easterling DR, Gleason B. Maximum and minimum temperature trends for the globe: An update through 2004. In: *Geophys. Res. Lett.* 2005;32:L23822.  
DOI: 10.1029/2005GL024379
- [24] Gao Y, Leung LR, Lu J, Liu Y, Huang M, Qian Y. Robust spring drying in the southwestern U.S. and seasonal migration of wet/dry patterns in a warmer climate. In: *Geophys. Res. Lett.* 2014;41(5):17451751.  
DOI: 10.1002/2014GL059562
- [25] Greene AM, Seager R. Categorical representation of North American precipitation projections. In: *Sci. Rep.* 2016;6:23888.  
DOI: 10.1038/srep23888
- [26] Ting M, Seager R, Li C, Liu H, Henderson N. Mechanism of Future Spring Drying in the Southwest U.S. in CMIP5 Models. In: *J. Climate.* 2018;31:42654279.  
DOI: 10.1175/JCLI-D-17-0574.1
- [27] Dai A, Trenberth KE, Qian T. A global dataset of palmer drought severity index for 18702002: Relationship with soil moisture and effects of surface warming. In: *J. Hydrometeorol.* 2004;5:11171130.
- [28] Greene AM, Goddard L, Gonzalez PL, Ines AV, Chryssanthacopoulos J. A climate generator for agricultural planning in southeastern South America. In: *Agr. Forest. Meteorol.* 2015;203:217228.  
DOI: 10.1016/j.agrformet.2015.01.008
- [29] Ford TW, Quiring SM, Frauenfeld OW. Multi-decadal variability of soil moisture temperature coupling over the contiguous United States modulated by Pacific and Atlantic sea surface temperatures. In: *Int. J. Climatol.* 2017;37(3):14001415.  
DOI: 10.1002/joc.4785
- [30] Cook BI, Seager R, Miller RL. Atmospheric circulation anomalies during two persistent north american droughts: 19321939 and 1948 1957. In: *Climate Dynamics.*

- 2011;36(11):23392355.  
DOI: 10.1007/s00382-010-0807-1
- [31] Seager R, Goddard L, Nakamura J, Henderson N, Lee DE. Dynamical causes of the 2010/11 Texas-Northern Mexico drought. In: *J. Hydrometeorol.* 2014;15:3968. DOI: 10.1175/JHM-D-13-024.1
- [32] Newman M, Alexander MA, Ault TR, Cobb KM, Deser C, Di Lorenzo E, et al. The Pacific decadal oscillation, revisited. In: *J. Climate.* 2016;29(12):43994427. DOI: 10.1175/JCLI-D-15-0508.1
- [33] Kerr RA. A North Atlantic climate pacemaker for the centuries. In: *Science.* 2000;288(5473):19841985. DOI: 10.1126/science.288.5473.1984
- [34] Knight JR, Allan RJ, Folland CK, Vellinga M, Mann ME. A signature of persistent natural thermohaline circulation cycles in observed climate. In: *Geophys. Res. Lett.* 2005;32(2005):L20708. DOI: 10.1029/2005GL024233
- [35] Alexander MA, Kilbourne KH, Nye JA. Climate variability during warm and cold phases of the Atlantic Multidecadal Oscillation (AMO) 1871-2008. In: *J. Marine Sys.* 2014;133:1426. DOI: <https://doi.org/10.1016/j.jmarsys.2013.07.017>
- [36] Higgins RW, Leetmaa A, Xue Y, Barnston A. Dominant factors influencing the seasonal predictability of U.S. precipitation and surface air temperature. In: *J. Climate.* 2000;13(22):39944017. DOI: 10.1175/1520-0442(2000)013<3994:DFITSP>2.0.CO;2
- [37] Zhang Y, Wallace JM, Battisti DS. ENSO-like interdecadal variability: 1900-93. In: *J. Climate.* 1997;10(5):10041020. DOI: 10.1175/1520-0442(1997)010<1004:ELIV>2.0.CO;2
- [38] Liu Z, Alexander M. Atmospheric bridge, oceanic tunnel and global climatic teleconnections. In: *Rev. Geophys.* 2007;45(2). DOI: 10.1029/2005RG000172
- [39] Seager R, Harnik N, Robinson WA, Kushnir Y, Ting M, Huang HP, et al. Mechanisms of ENSO-forcing of hemispherically symmetric precipitation variability. In: *Q.J. Royal Meteorol. Soc.* 2005;131(608):15011527. DOI: 10.1256/qj.04.96
- [40] Seager R, Naik N, Ting M, Cane MA, Harnik N, Kushnir Y. Adjustment of the atmospheric circulation to tropical Pacific SST anomalies: Variability of transient eddy propagation in the Pacific-North America sector. In: *Q.J. Royal Meteorol. Soc.* 2010;136(647):277296. DOI: 10.1002/qj.588
- [41] Gershunov A, Barnett TP. Interdecadal modulation of ENSO teleconnection. In: *Bull. Am. Met. Soc.* 1998;79(12):27152725.
- [42] Seager R, Hoerling M, Schubert S, Wang H, Lyon B, Kumar A, et al. Causes of the 2011-14 California drought. In: *J. Climate.* 2015;28(18):69977024. DOI: 10.1175/JCLI-D-14-00860.1
- [43] Cook BI, Smerdon JE, Seager R, Coats S. Global warming and 21st century drying. In: *Clim. Dyn.* 2014;43(9-10):26072627. DOI: 10.1007/s00382-014-2075-y
- [44] Seager R, Ting M, Held I, Kushnir Y, Lu J, Vecchi G, et al. Model projections of an imminent transition to a more arid climate in Southwestern North America. In: *Science.* 2007;316(5828):11811184. DOI: 10.1126/science.1139601
- [45] Meehl GA, Goddard L, Murphy J, Stouffer RJ, Boer G, Danabasoglu G, et al. Decadal prediction. In: *Bull. Am. Meteorol. Soc.* 2009;90(10):14671486. DOI: 10.1175/2009BAMS2778.1
- [46] Solomon A, Goddard L, Kumar A, Carton J, Deser C, Fukumori I, et al. Distinguishing the roles of natural and anthropogenically forced decadal climate variability. In: *Bull. Am. Meteorol. Soc.* 2011;92(2):141156. DOI: 10.1175/2010BAMS2962.1
- [47] Goddard L, Kumar A, Solomon A, Smith D, Boer G, Gonzalez P, et al. A verification framework for interannual-to-decadal predictions experiments. In: *Clim. Dyn.* 2013;40(1):245272. DOI: 10.1007/s00382-012-1481-2
- [48] Seager R, Ting M. Decadal drought variability over North America: Mechanisms

- and predictability. In: Curr. Clim. Change Rep. 2017;3(2):141149.  
DOI: 10.1007/s40641-017-0062-1
- [49] Cayan DR, Das T, Pierce DW, Barnett TP, Tyree M, Gershunov A. Future dryness in the southwest US and the hydrology of the early 21st century drought. In: P. Natl. Acad. Sci. 2010;107(50):2127121276.  
DOI: 10.1073/pnas.0912391107
- [50] Seager R, Naik N, Vogel L. Does globalwarming cause intensified interannual hydroclimate variability? In: J. Climate. 2012;25(9):33553372.  
DOI: 10.1175/JCLI-D-11-00363.1
- [51] Mankin JS, Smerdon JE, Benjamin I. C, Williams AP, Seager R. The curious case of projected twenty-first-century drying but greening in the AmericanWest. In: J. Climate. 2017;30:86898710.  
DOI: 10.1175/JCLI-D-17-0213.1
- [52] Mankin JS, Seager R, Smerdon JE, Cook BI, Williams AP, Horton RM. Blue water trade-offs with vegetation in a co2-enriched climate. In: Geophys. Res. Lett. 2018;45(7):31153125.  
DOI:10.1002/2018GL077051
- [53] Schlesinger WH, Lichter J. Limited carbon storage in soil and litter of experimental forest plots under increased atmospheric CO2. In: Nature. 2001;411:466469.  
DOI:10.1038/35078060

---

© 2020 Greene and Seager; This is an Open Access article distributed under the terms of the Creative Commons Attribution License (<http://creativecommons.org/licenses/by/4.0>), which permits unrestricted use, distribution and reproduction in any medium, provided the original work is properly cited.

*Peer-review history:*  
*The peer review history for this paper can be accessed here:*  
<http://www.sdiarticle4.com/review-history/56192>